A model for distortions of polarisation angle in radio pulsars[1]

L. Saha[1], J. Dyks[1], S. Oslowski[2,3], M. Serylak[4], L. Guillemot[5,6], I. Cognard[5,6] and B. Rudak[1]

[1] Nicolaus Copernicus Astronomical Center, Toruń, Poland
[2] Fakultät für Physik, Universität Bielefeld, Postfach 100131, 33501 Bielefeld, Germany
[3] Max-Planck-Institut für Radioastronomie, Auf dem Hügel 69, 53121 Bonn, Germany
[4] Universtity of the Western Cape, Cape Town, South Africa
[5] Laboratoire de Physique et Chimie de l'Environnement et de l'Espace LPC2E CNRS-Université d'Orléans, F-45071 Orléans, France
[6] Station de radioastronomie de Nançay, Observatoire de Paris, CNRS/INSU F-18330 Nançay, France

[1]A poster contribution to the "28th Texas Symposium on Relativistic Astrophysics", Geneva, Switzerland, 13-18 December 2015.

PSR B1821-24A (GBT)

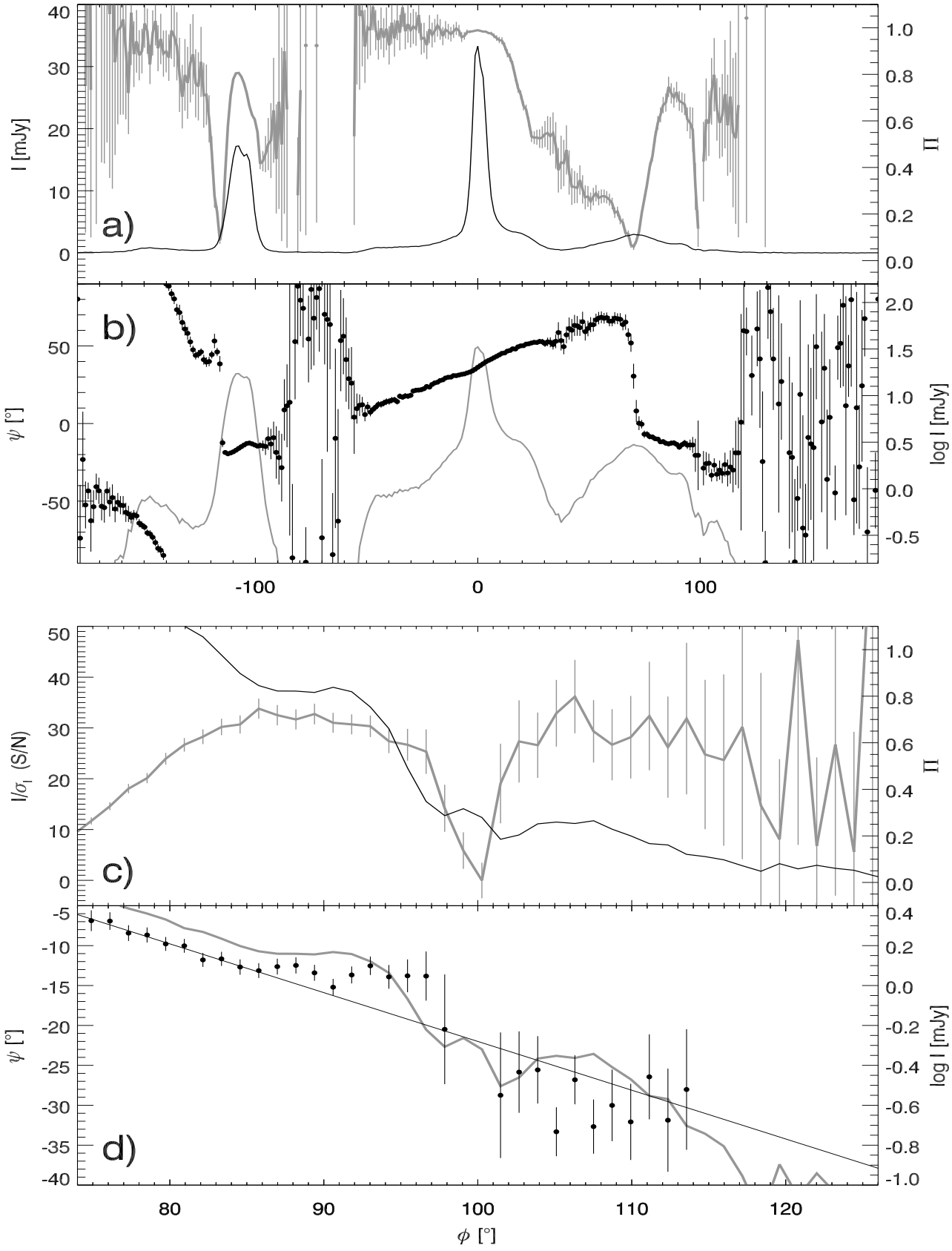

Figure 1: Linear polarization properties of PSR B1821-24A as observed with GBT in L band. **a)** Total flux I (black solid) and the linear polarisation fraction $\Pi = L/I$ (grey). **b)** The PA (black) and $\log I$ (grey). **c)** The total flux S/N (black solid) and the polarisation fraction (grey). **d)** The PA (black) and $\log I$ (grey). The straight line presents the PA variations anticipated in the absence of the notches. Note the drop of Π and the change of PA at the notches.

PSR B1821-24A (Nançay)

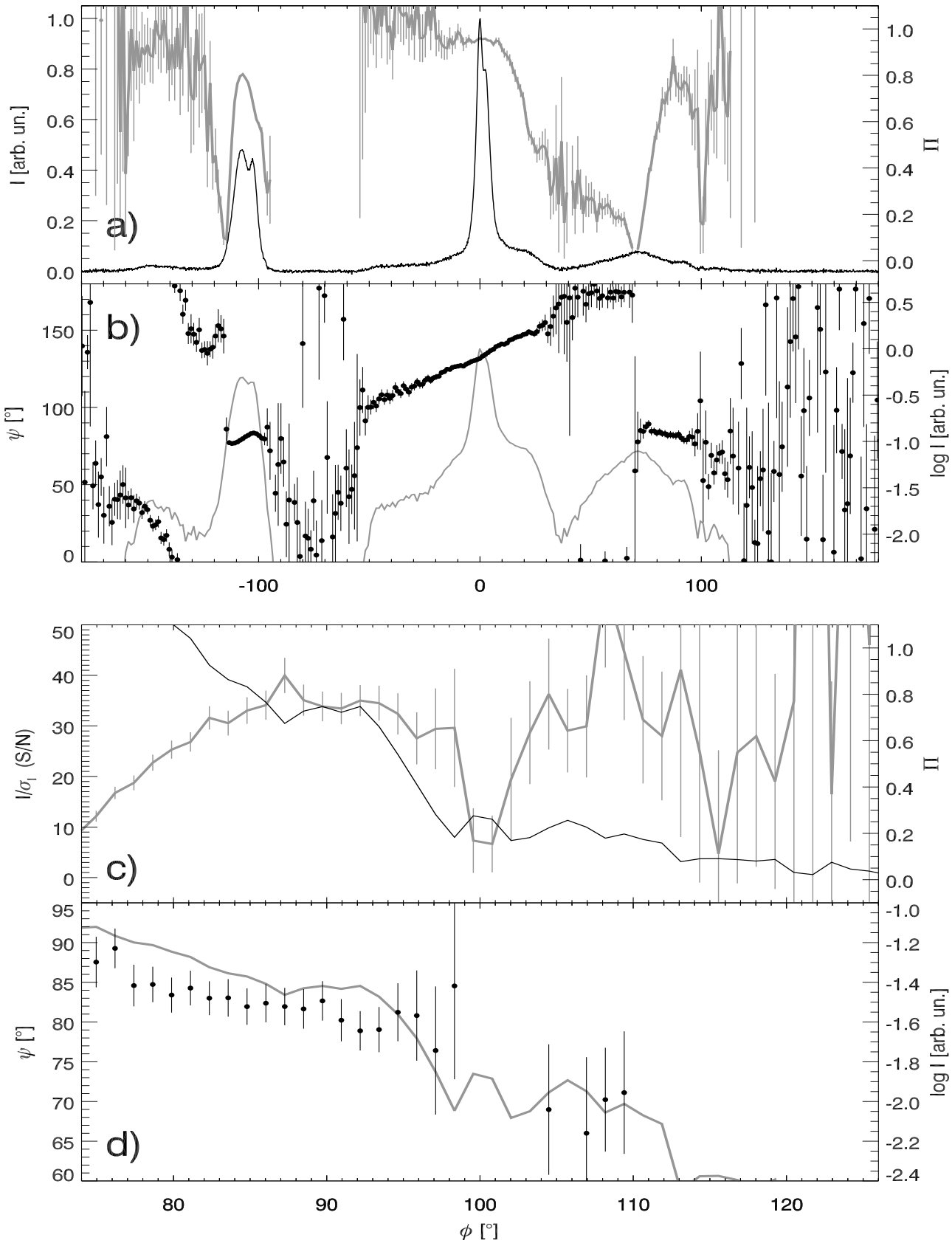

Figure 2: Linear polarisation properties of PSR B1821−24A observed at 1.5 GHz with the Nançay telescope. The layout is the same as in Fig. 1. The total profile in a) has 2048 samples per period P, whereas the other data are for seven adjacent bins merged (292 bins/P).

PSR J0437-4715 (Parkes)

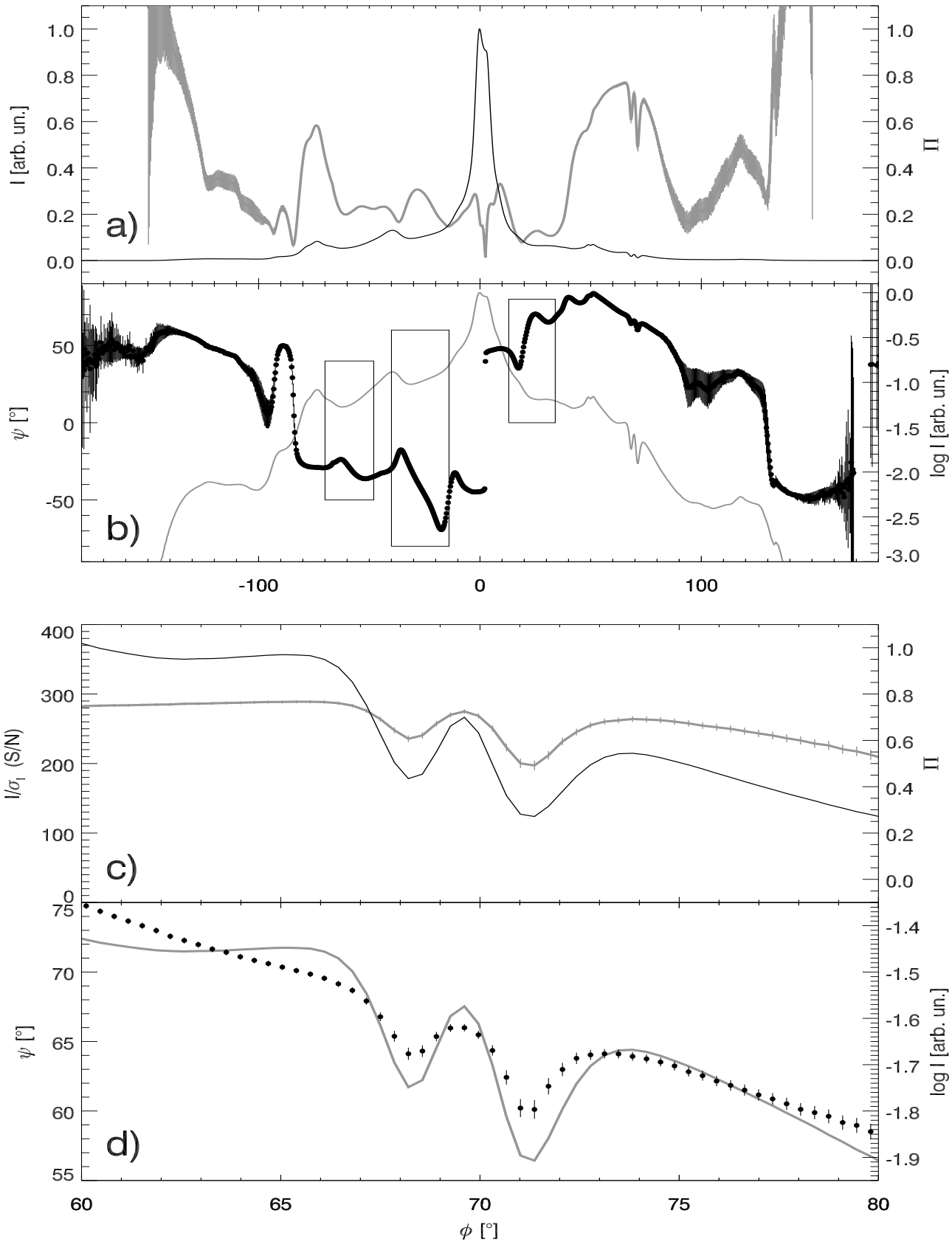

Figure 3: Linear polarization properties of PSR J0437-4715 observed at 1.4 GHz with the Parkes telescope. The layout is same as in previous figures. PA distortions are marked with rectangular boxes.

The bifurcated microbeam of our model

The whole microbeam is polarised at a fixed angle Ψ_B

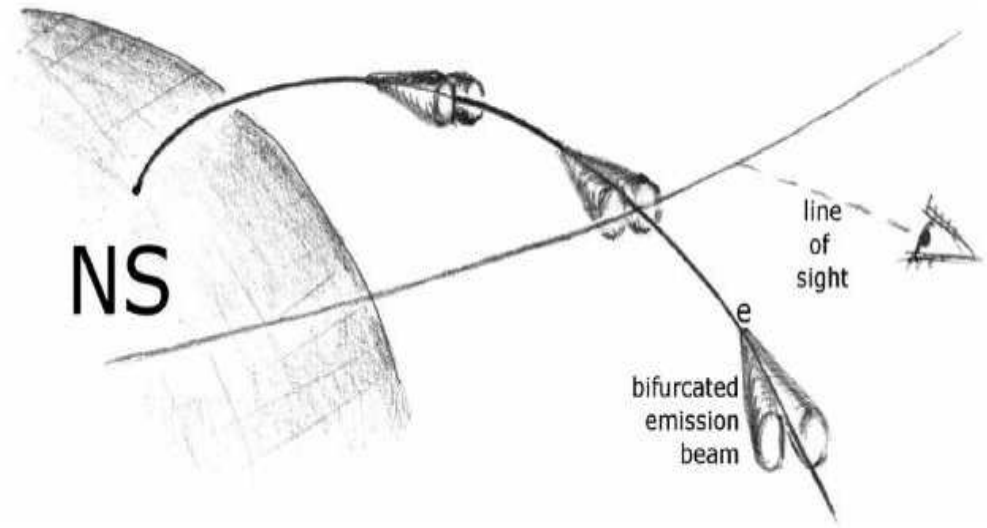

Figure 4: A single trajectory of electrons flowing in a stream of finite width resulting in a split-fan emission pattern.

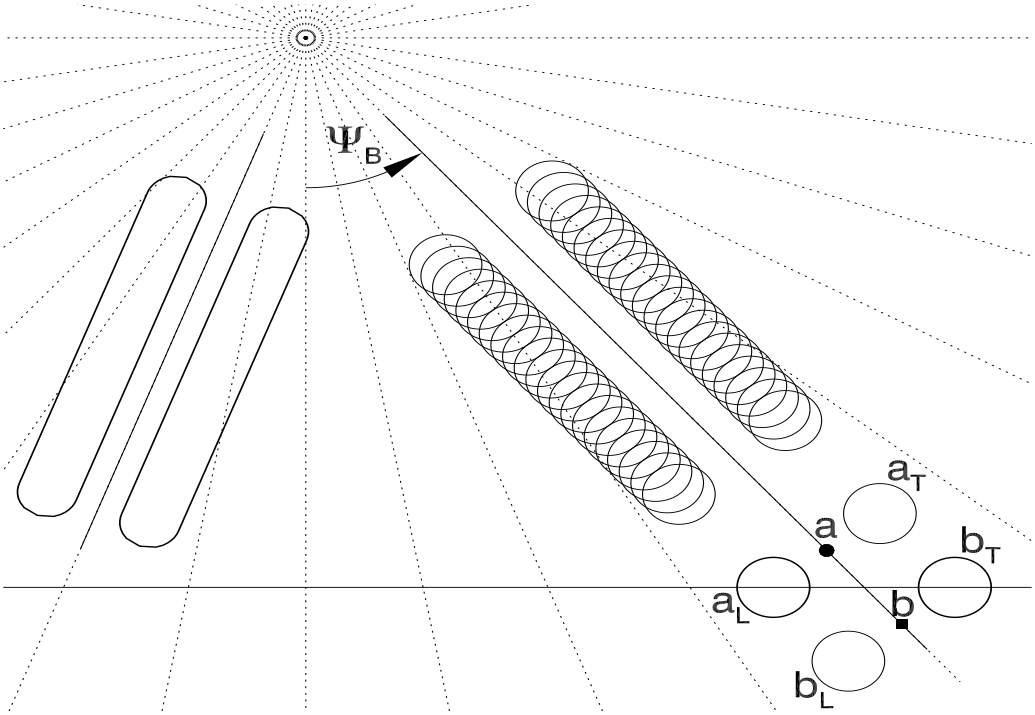

Figure 5: A sky-projected view of the split-fan beams typical of the X-mode curvature radiation from narrow plasma streams. The continuous beam shown on the left, can be decomposed into a sequence of lobe pairs, emitted quasi-instantaneously from different points along the stream (shown on the right-hand side), e.g. from the points 'a' and 'b' in the bottom-right corner. The horizontal line marks the passage of the line of sight. The stream's polarisation angle Ψ_B is detectable at two pulse longitudes (corresponding to the lobes a_L and b_T), on the leading and trailing side of the stream.

The polarization angle (PA) zigzag mechanism

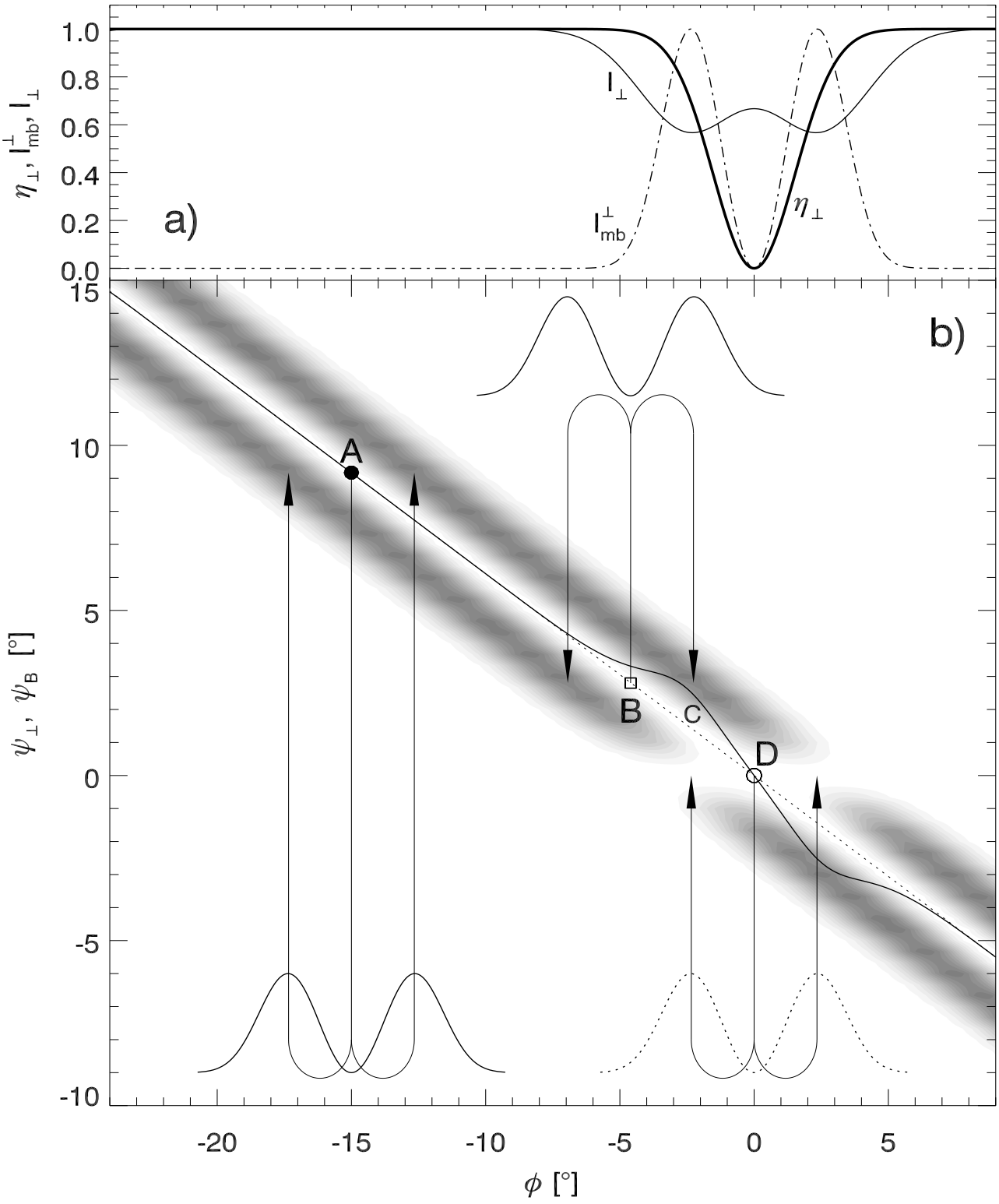

Figure 6: **a)** The effective microbeam pattern $I^\perp_{\rm mb}$ (dot-dashed), and the macroscopic X-mode emissivity $\eta_\perp$ (thick solid) are convolved into the net intensity profile $I_\perp$ (thin solid). **b)** The PA as a function of phase. The slanted solid line marks $\psi_\perp$, i.e. the net value of the X-mode PA, calculated as a fixed-phase average of the bifurcated grey band. Dotted line marks the RVM-based reference (ψ_B). The double-peaked microbeams, with arrows emerging from points A and B, present how the PA is distributed within the neighbouring pulse longitudes. The void assumed in $\eta_\perp$ at D ($\phi = 0$), creates the horizontal break in the bifurcated PA band (grey). The resulting imbalance of the PA averaging produces the thick solid PA wiggle

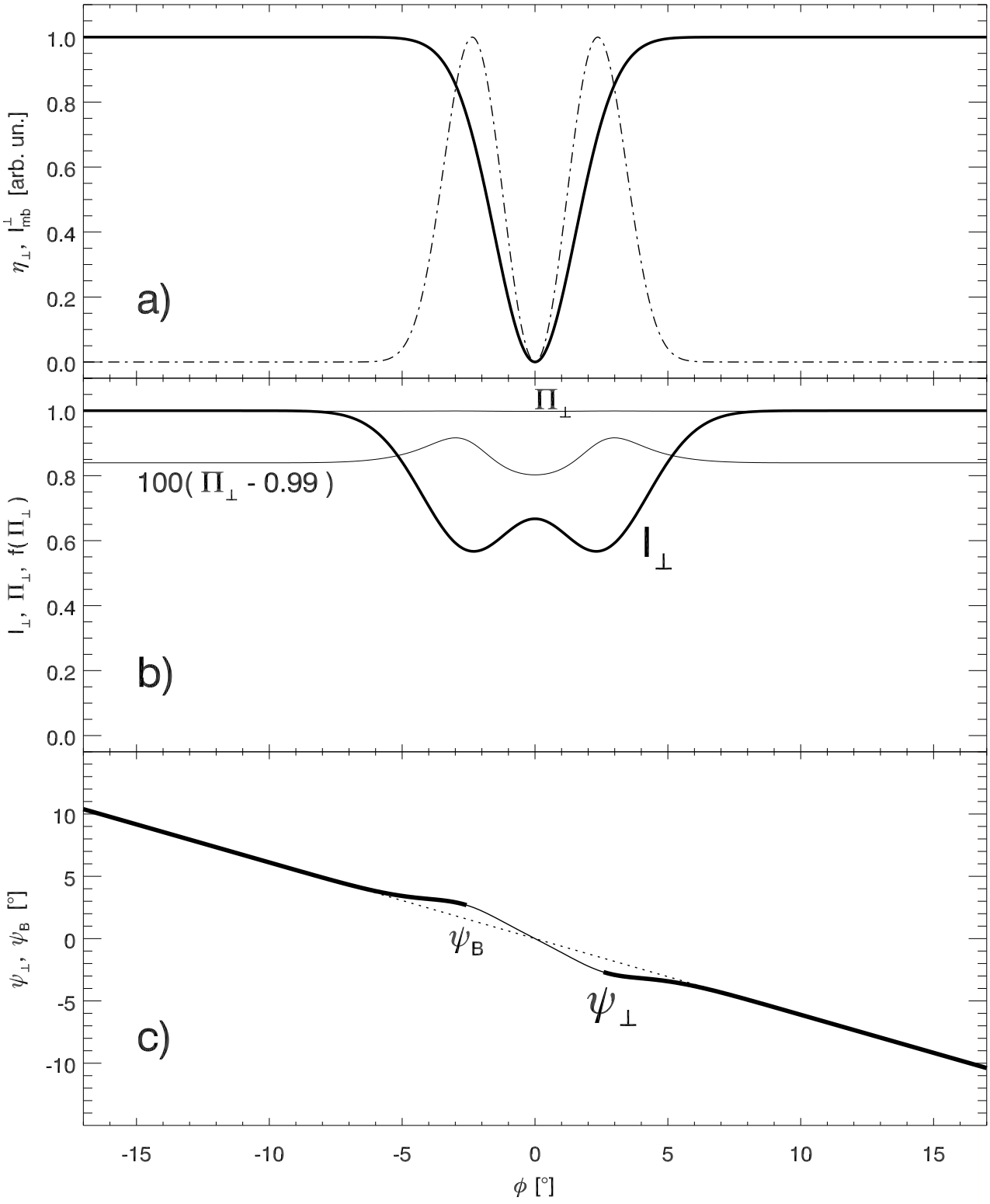

Figure 7: A sample result of a calculation which produces the PA wiggle at a nearly merged double notch feature. **a)** The microbeam intensity $I^\perp_{\rm mb}$ (dot-dashed) and the macroscopic emissivity with a Gaussian cavity at $\phi = 0$ (thick solid). **b)** The net polarisation fraction $\Pi_\perp$ (top thin solid line) and the net X-mode intensity profile (thick solid). The $\Pi_\perp$ is slightly smaller than 1, as shown by the bottom thin line presenting the quantity $100(\Pi_\perp - 0.99)$. **c)** The net X-mode PA ($\psi_\perp$, solid), overplotted on the reference ψ_B (dotted). The central part of $\psi_\perp$ is thinner to reflect the lack of high-quality data points at the center of notches in B1821−24A (see Figs. 1d). The result is for $\sigma_\eta = 1.53°$, $\psi_B = -0.6\phi$, $\rho_{\rm crv} = 5 \times 10^4$ cm, and $\nu = 1$ GHz.

Ordinary mode (O-mode) added

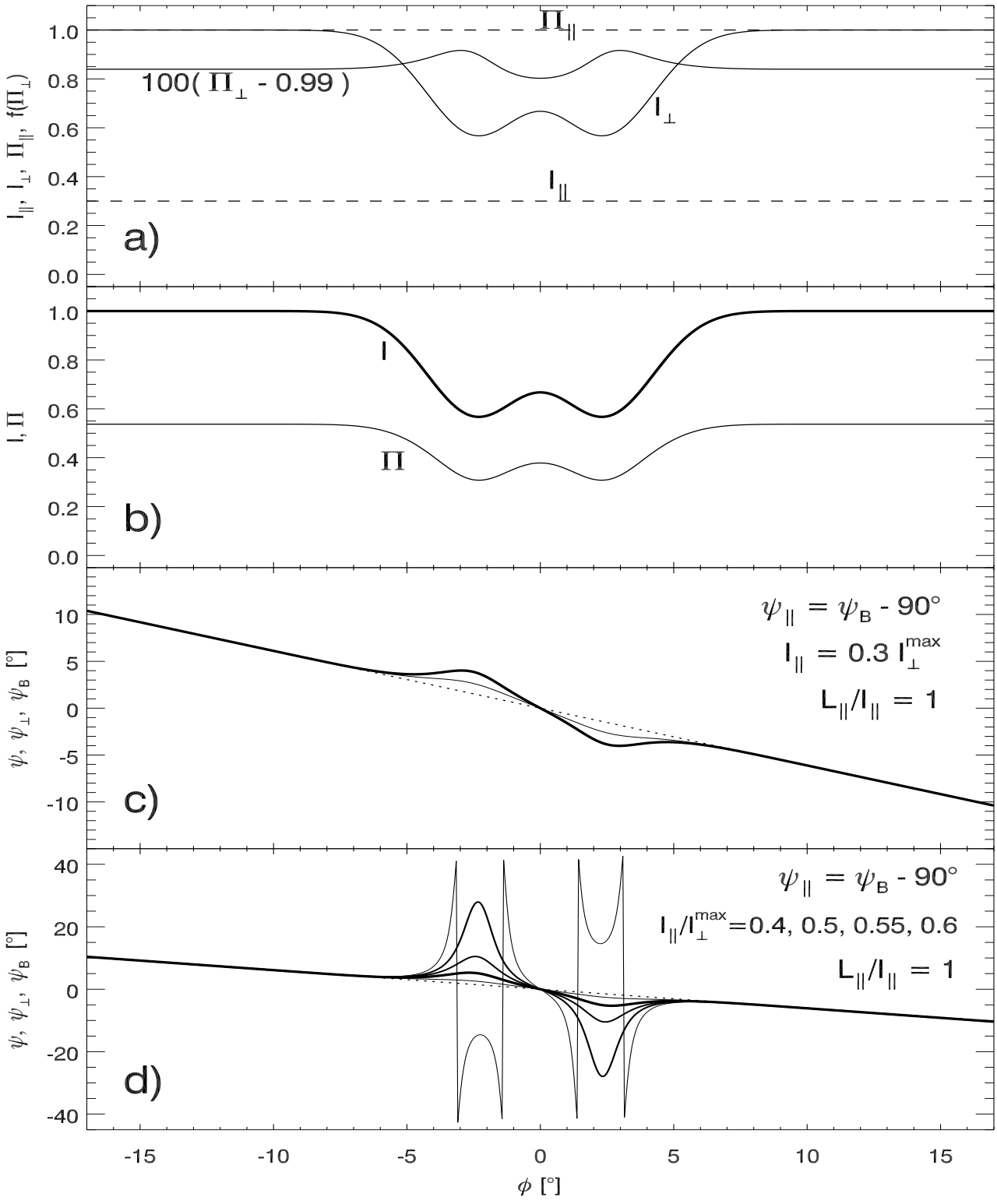

Figure 8: Polarisation of double notches in the presence of two polarisation modes (X-mode and O-mode. **a)** Intensity and polarisation fraction for both modes ($\perp$-mode: solid; $\parallel$-mode: dashed). $\Pi_\perp$ is indiscernible from $\Pi_\parallel = 1$, hence we plot $100(\Pi_\perp - 0.99)$. **b)** Total intensity (thick solid) and the total Π (thin). **c)** The total PA ψ (thick solid) overplotted on the net PA of the X-mode ($\psi_\perp$, thin solid), and the reference ψ_B of the RVM model (dotted). Note how the contribution of the O mode increases the off-RVM amplitude of the total PA. **d)** Same as in c, but for the increasing contribution of the O mode: $I_\parallel/I_\perp^{\rm max} = 0.4$, 0.5, 0.55, and 0.6. The last case (thin line with spikes) undergoes the orthogonal-mode jumps. Unspecified parameters are the same as in Fig. 7.

Quasi-orthogonal modes

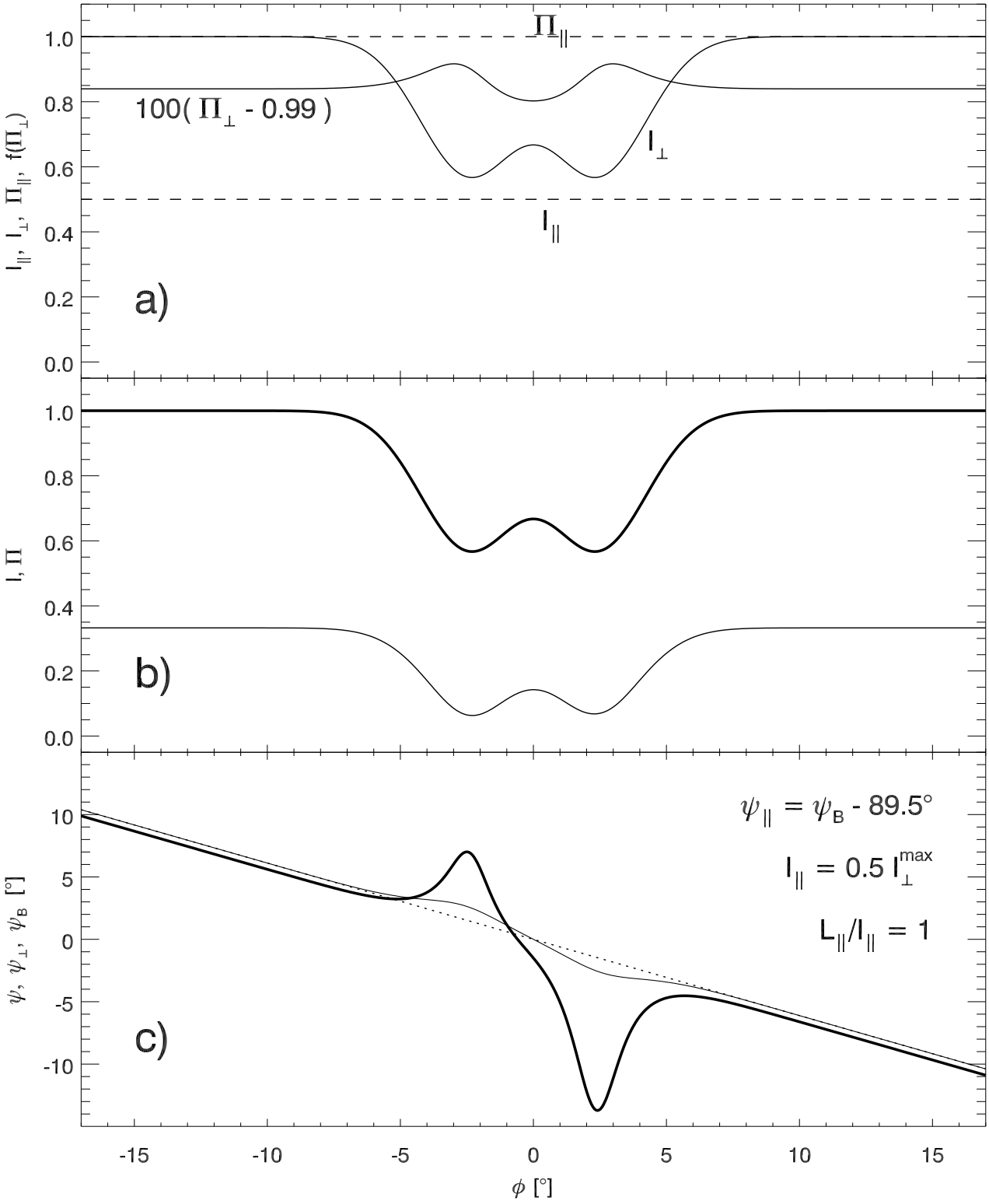

Figure 9: Polarisation of double notches in the presence of a considerable amount of a quasi-orthogonal secondary polarisation mode ($\psi_\parallel = \psi_B - 89.5°$, $I_\parallel = 0.5 I_\perp^{\max}$). The layout is the same as in panels a-c of Fig. 8. Note the large amplitude and asymmetry of the PA wiggle in panel c. Nonspecified parameters are the same as before.

A model for J0437−4715 (cf. Fig. 3)

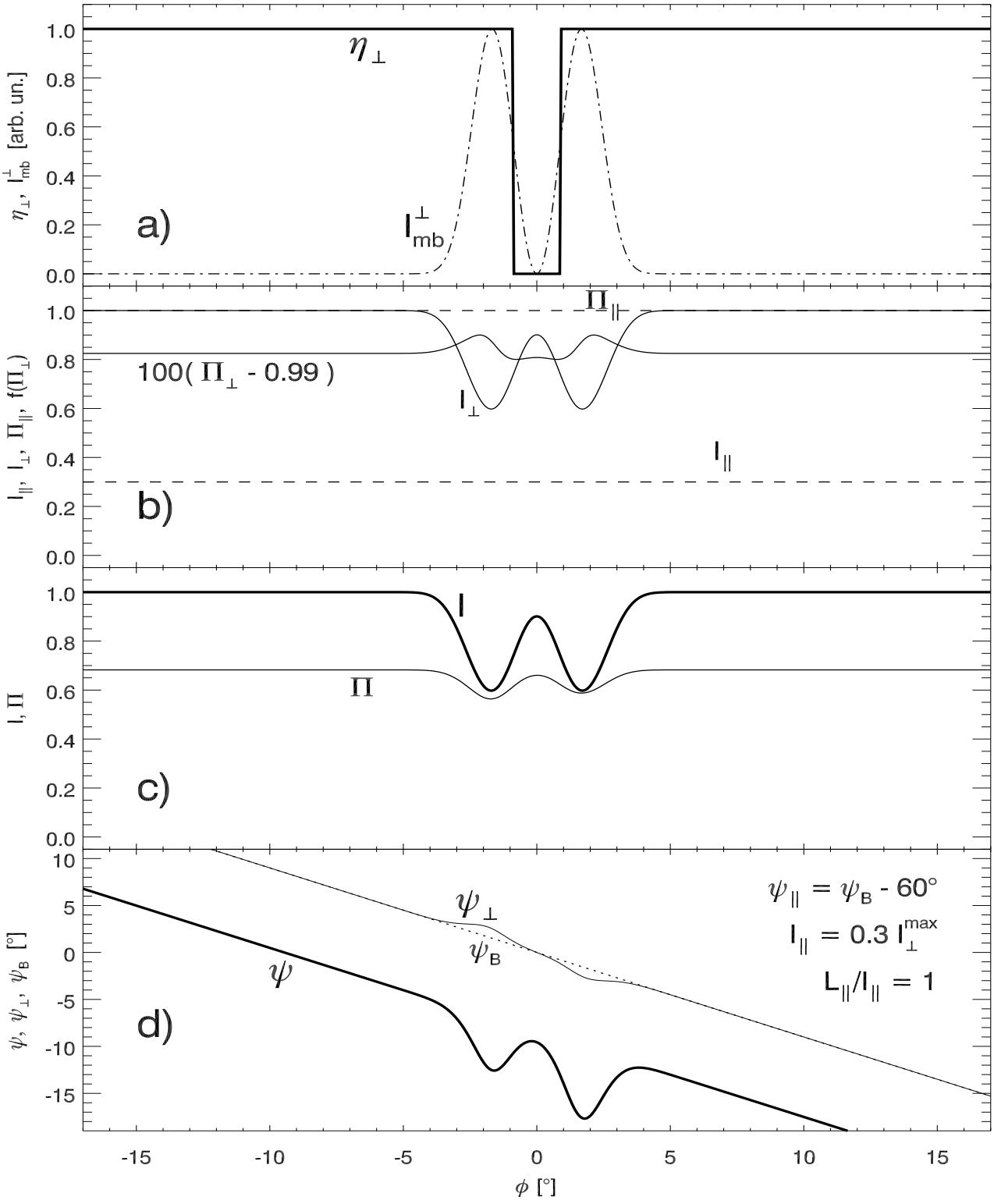

Figure 10: Model results aimed at reproducing the observed properties of the double notches in J0437−4715 (see Fig. 3). A rectangular void in emissivity, of a half-width equal to 0.9° (thick line in a), has been assumed to raise the central maximum of I at $\phi = 0$. The layout of panels b-d is analogous to panels a-c in Fig. 8. List of parameters: $\psi_B = -0.9\phi$, $\psi_\parallel = \psi_B - 60°$, $I_\parallel = 0.3 I_\perp^{\rm max}$, $\rho_{\rm crv} = 1.4 \times 10^5$ cm, $\nu = 1$ GHz.

How the zigzag is transformed into “W”

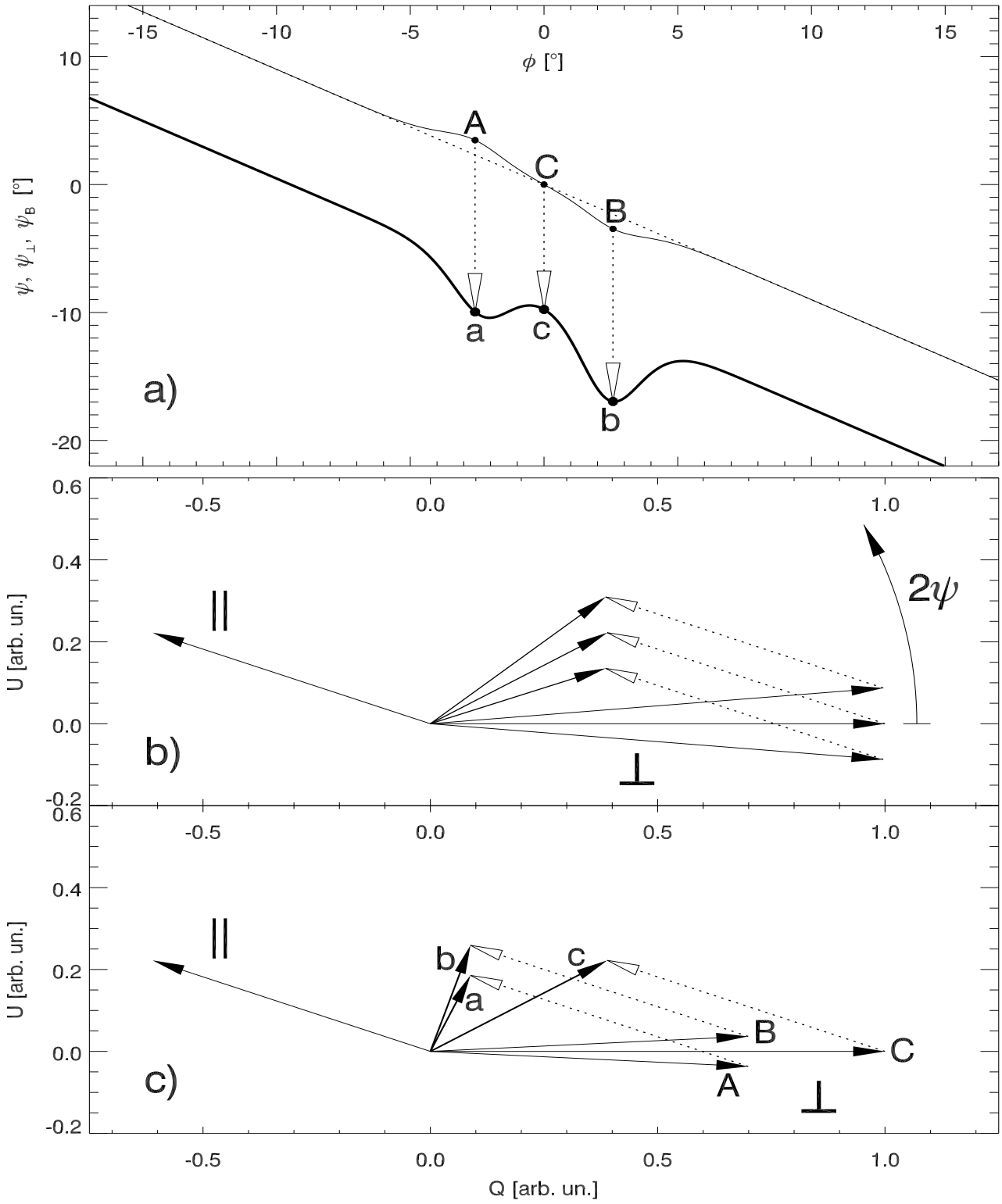

Figure 11: The mechanism of transformation of the bidirectional PA distortion (the thin solid X-mode wiggle in panel a) into a one-directional W-shaped deflection of the total PA (thick solid). The Stokes vectors associated with the marked points are shown schematically in panel c. Those with small letters (a, b, c) are the sum of the corresponding X-mode vectors (A, B, C) with the quasi-orthogonal ||-mode vector shown on the left. The transition to the W-shaped PA is mainly caused by the drop of the X-mode flux at the minima of double notches (short vectors A and B). Panel b presents a similar sum for the case with no drop of polarised flux at A and B (all ⊥-mode vectors have the same length).

Bifurcated emission component in J0437−4715

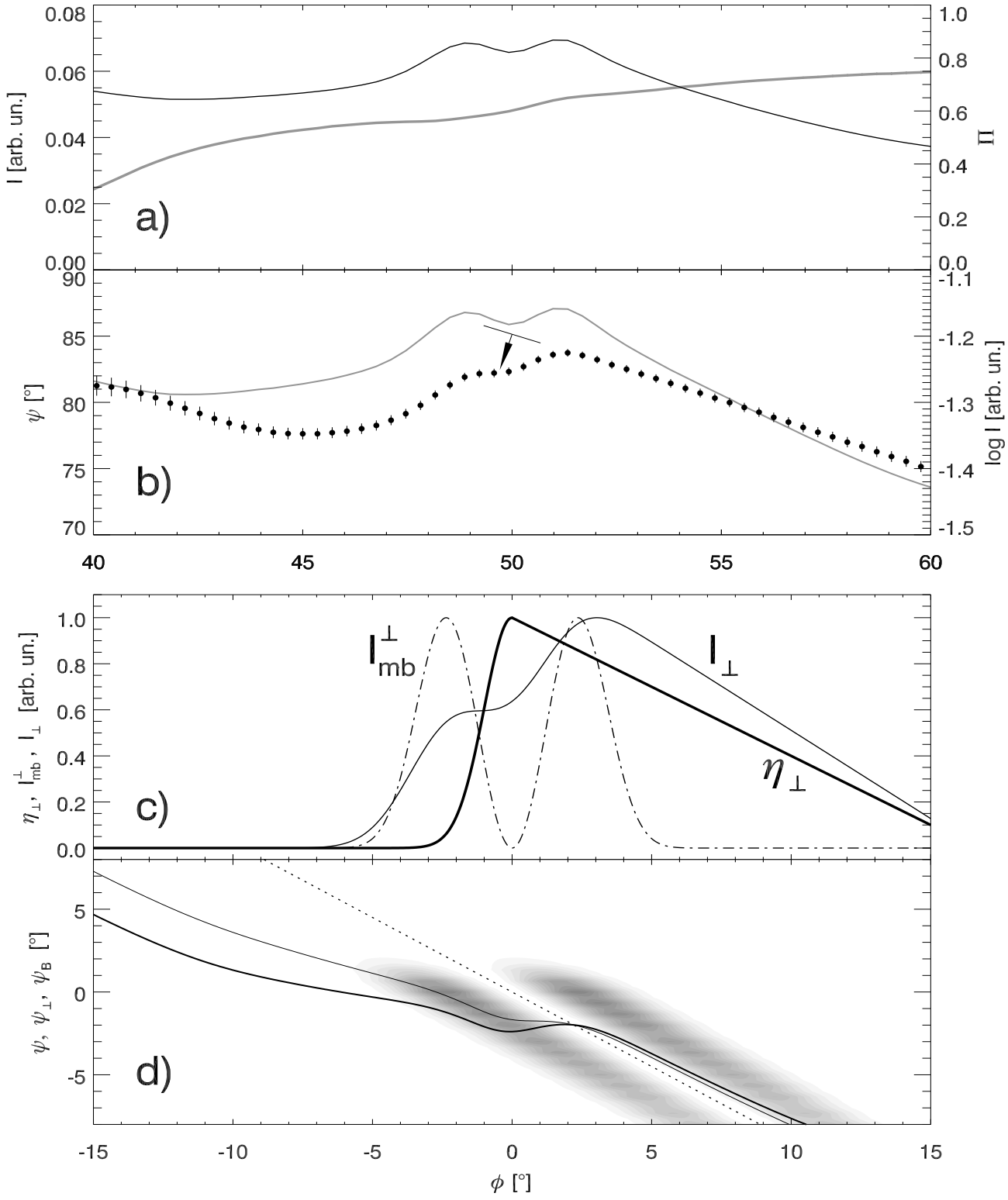

Figure 12: Comparison of the observed (panels a and b) and modelled (c and d) properties of the bifurcated trailing component (BTC) in J0437−4715. The observed properties (I and Π in **a**; ψ and $\log I$ in **b**) present a zoomed part of Fig. 3. The arrow in b marks a step-like change of PA at the center of the BTC (the PA is shown with dots). A similar step-like change of PA (solid lines in panel d) occurs for a one-sided emissivity profile ($\eta_\perp$, thick solid in c) which is decreasing gradually (linearly) on the right-hand side, whereas much more steeply on the left-hand side (a half-Gaussian with $\sigma_\eta = 1°$). Thin solid line in d presents $\psi_\perp$, whereas the thick line presents ψ obtained for a fixed fractional contribution of the O mode: $I_\parallel = 0.3 I_\perp(\phi)$. This is an exemplary result obtained for $\psi_B = -0.9\phi$, $\rho_{\rm crv} = 5 \times 10^4$ cm.

Data Courtesy

GBT

- Bilous, A. V., Pennucci, T. T., Demorest, P., Ransom, S. M., 2015, ApJ, 803, 83

Parkes

- Dai, S., Hobbs, G., Manchester, R. N., et al., 2015
- Osłowski, S., van Straten, W., Bailes, M., Jameson, A., Hobbs, G., 2014, MNRAS, 441, 3148